LETTER

Corrected: Author Correction

https://doi.org/10.1038/s41586-019-0924-x

Spatial and temporal heterogeneity of mouse and human microglia at single-cell resolution

Takahiro Masuda[1,17], Roman Sankowski[1,2,17], Ori Staszewski[1,17], Chotima Böttcher[3], Lukas Amann[1,4], Sagar[6], Christian Scheiwe[5], Stefan Nessler[7], Patrik Kunz[7], Geert van Loo[8,9], Volker Arnd Coenen[10], Peter Christoph Reinacher[10], Anna Michel[11], Ulrich Sure[11], Ralf Gold[12], Dominic Grün[6], Josef Priller[3,13,14], Christine Stadelmann[7] & Marco Prinz[1,15,16]*

Microglia have critical roles not only in neural development and homeostasis, but also in neurodegenerative and neuroinflammatory diseases of the central nervous system[1–4]. These highly diverse and specialized functions may be executed by subsets of microglia that already exist in situ, or by specific subsets of microglia that develop from a homogeneous pool of cells on demand. However, little is known about the presence of spatially and temporally restricted subclasses of microglia in the central nervous system during development or disease. Here we combine massively parallel single-cell analysis, single-molecule fluorescence in situ hybridization, advanced immunohistochemistry and computational modelling to comprehensively characterize subclasses of microglia in multiple regions of the central nervous system during development and disease. Single-cell analysis of tissues of the central nervous system during homeostasis in mice revealed specific time- and region-dependent subtypes of microglia. Demyelinating and neurodegenerative diseases evoked context-dependent subtypes of microglia with distinct molecular hallmarks and diverse cellular kinetics. Corresponding clusters of microglia were also identified in healthy human brains, and the brains of patients with multiple sclerosis. Our data provide insights into the endogenous immune system of the central nervous system during development, homeostasis and disease, and may also provide new targets for the treatment of neurodegenerative and neuroinflammatory pathologies.

Recent whole transcriptome analyses of the development of microglia from yolk sac progenitors to adult microglia have highlighted the degree to which cells change during this interval, and revealed marked differences in gene expression between early postnatal periods and adulthood[5–7]. However, recent single-cell RNA sequencing (scRNA-seq) studies of microglia have either only used pre-sorted myeloid cell populations[8,9] or whole brain approaches[10], without addressing the possibility of spatially and temporally restricted subtypes of microglia in several regions of the central nervous system (CNS). To study the heterogeneity of microglia at a single-cell level during different homeostatic conditions, we analysed single microglial cells from multiple anatomical regions of the embryonic (embryonic day (E)16.5), juvenile (3 weeks) and adult (16 weeks) mouse CNS (Extended Data Fig. 1a, Supplementary Fig. 1). The areas of the CNS were selected to match those that have previously been found to exhibit transcriptional differences of microglial bulk RNA on Affymetrix analysis[11]. To compare expression patterns during homeostasis to those under pathological conditions, microglia were also isolated from mice with neurodegenerative (facial nerve axotomy) and demyelinating (cuprizone) pathologies (Extended Data Fig. 1a). Following quality control, data from a total of 3,826 single microglia were further analysed using the RaceID algorithm[12] and finally depicted in *t*-distributed stochastic neighbour embedding (*t*-SNE) plots (Extended Data Fig. 1b, d). Unsupervised clustering gave rise to 13 distinct clusters, corresponding to the ten microglia clusters present during development (C1 to C10), as well as one cluster for neurodegeneration (C11) and two clusters for demyelination and remyelination (C12 and C13) (Extended Data Fig. 1c).

To gain insight into the diversity of microglia during development, we first focused on microglia from non-diseased CNS tissue. The *t*-SNE plots displayed two main clouds that clearly segregate embryonic and postnatal microglia (Fig. 1a). Unbiased clustering revealed the presence of ten major clusters (the C1 to C10 referred to above) with distinct transcriptional profiles (Fig. 1b, c). Clusters C1 to C6 predominantly consisted of embryonic microglia, whereas the postnatal microglia constituted clusters C7 to C10 (Fig. 1a, b). Notably, the embryonic clusters were differentially distributed across the four regions of the embryonic CNS (Fig. 1d, e). Likewise, the postnatal clusters showed a variable distribution both spatially and temporally; for example, C10 was enriched in juvenile cortical and hippocampal microglia, and the minor cluster C7 was more prevalent in the cerebellum and corpus callosum of adult mice (Fig. 1d, e). The relative proportion of clusters in the cerebellum did not change between the juvenile and the adult stages, which is in sharp contrast to what was observed in the cortex and hippocampus (Fig. 1d, e). As compared to juvenile microglia, adult microglia showed a more homogenous distribution of each cluster across regions (Fig. 1d, e). Together, these data suggest different subtypes of microglia with distinct gene expressional profiles exist over the course of development, with strong variation between different regions of the CNS that might reflect local specification.

Among the top differentially regulated genes during development were the microglial homeostatic genes *Tmem119*, *Selplg* and *Slc2a5*, which are highly expressed in postnatal microglia (Fig. 2a). The expression of *Malat1*, a long non-coding RNA, also increased during development (Extended Data Fig. 2a, b). In the embryonic clusters, the lysosome-related genes *Ctsb* (which encodes cathepsin B), *Ctsd* (which encodes cathepsin D) and *Lamp1* (which encodes lysosomal-associated membrane protein 1) were strongly expressed in C1 and C2 microglia (Fig. 2b, Extended Data Fig. 2c), which suggests that lysosomal activity is enhanced in these embryonic microglia. Expression of *Apoe*, which encodes the myeloid cell activation marker apolipoprotein E (APOE)[13], was enriched in the C1, C4 and C5 clusters (Fig. 2b). C6 microglia were characterized by high levels of expression of *Tmsb4x*, *Eef1a1* and *Rpl4*

[1]Institute of Neuropathology, Medical Faculty, University of Freiburg, Freiburg, Germany. [2]Berta-Ottenstein-Programme for Clinician Scientists, Faculty of Medicine, University of Freiburg, Freiburg, Germany. [3]Department of Neuropsychiatry and Laboratory of Molecular Psychiatry, Charité – Universitätsmedizin Berlin, Berlin, Germany. [4]Faculty of Biology, University of Freiburg, Freiburg, Germany. [5]Clinic for Neurosurgery, Faculty of Medicine, University of Freiburg, Freiburg, Germany. [6]Max Planck Institute of Immunobiology and Epigenetics (MPI-IE), Freiburg, Germany. [7]Institute of Neuropathology, University Medical Center Göttingen, Göttingen, Germany. [8]VIB Center for Inflammation Research, Ghent, Belgium. [9]Department of Biomedical Molecular Biology, Ghent University, Ghent, Belgium. [10]Department of Stereotactic and Functional Neurosurgery, Medical Faculty, University of Freiburg, Freiburg, Germany. [11]Department of Neurosurgery, University Hospital Essen, Essen, Germany. [12]Department of Neurology, St. Josef Hospital, Ruhr University Bochum, Bochum, Germany. [13]DZNE, Berlin, Germany. [14]UK DRI, University of Edinburgh, Edinburgh, UK. [15]Signalling Research Centres BIOSS and CIBSS, University of Freiburg, Freiburg, Germany. [16]Center for NeuroModulation, Faculty of Medicine, University of Freiburg, Frieburg, Germany. [17]These authors contributed equally: Takahiro Masuda, Roman Sankowski, Ori Staszewski. *e-mail: marco.prinz@uniklinik-freiburg.de

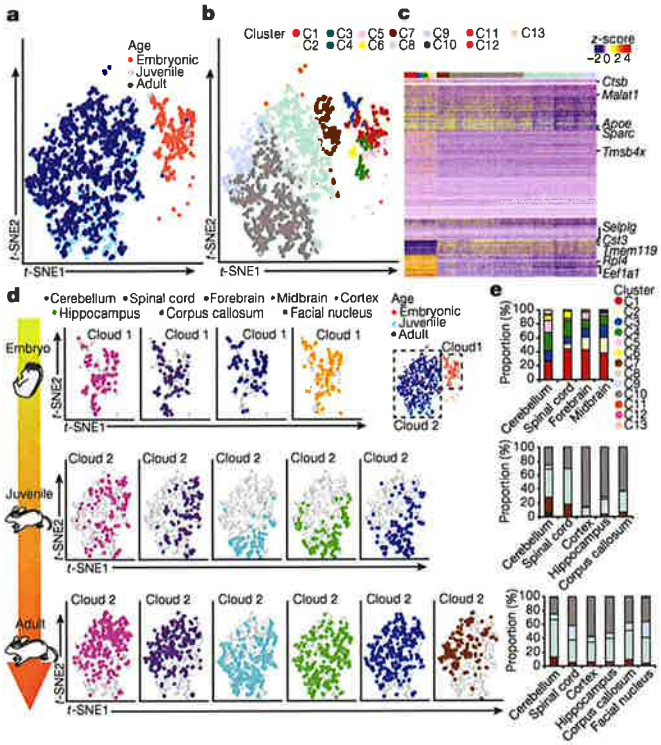

Fig. 1 | Identification of spatiotemporal subclasses of microglia in the mouse. a, *t*-SNE plot of 2,966 individual microglia at different time points of development. Each dot represents a single cell. Colours correspond to the developmental stages investigated. **b**, *t*-SNE plot depicting ten major and three minor clusters at three different developmental stages. Colours represent each cluster. **c**, Heat map of the top differentially regulated genes in each cluster. **d**, *t*-SNE plots depicting regional distribution of transcripts from 2,966 individual microglia at different developmental time points. **e**, Distribution of microglia clusters across different regions of the CNS during embryonic and postnatal stages.

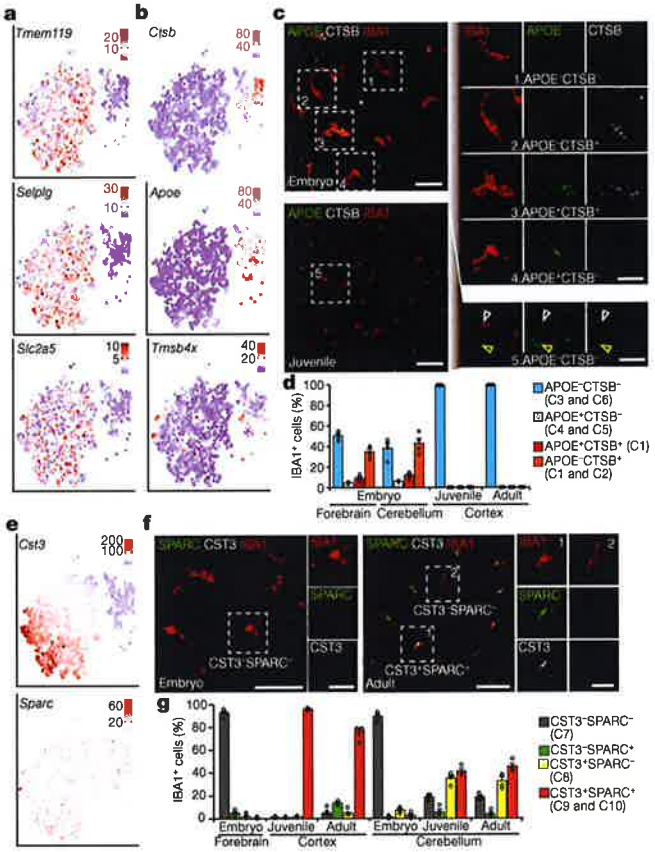

Fig. 2 | Characteristics of subsets of microglia during development. a, *t*-SNE plots depicting the expression kinetics of the microglial core genes *Tmem119*, *Selplg* and *Slc2a5* during ontogeny (2,966 cells). Colour key indicates the expression levels. **b**, *t*-SNE plots (2,966 cells) of embryo-enriched microglial transcripts for *Ctsb*, *Apoe* and *Tmsb4x*. **c**, Representative immunofluorescence images for APOE, CTSB and IBA1 in the embryonic forebrain and juvenile cortex. Inset 1 (dashed frame) indicates APOE$^-$CTSB$^-$IBA1$^+$ microglia (representing clusters C3 and C6). Inset 2 illustrates APOE$^-$CTSB$^+$IBA1$^+$ microglia (C1 and C2) and inset 3 shows APOE$^+$CTSB$^+$IBA1$^+$ microglia (C1). Inset 4 depicts APOE$^+$CTSB$^-$IBA1$^+$ microglia (C4 and C5). Inset 5 illustrates APOE$^-$CTSB$^-$IBA1$^+$ microglia (white arrowheads) found at the juvenile stage. Yellow arrowheads indicate APOE$^+$IBA1$^-$ juvenile microglia. Representative images out of four investigated mice are shown. Scale bars, 50 μm (overview), 30 μm (insets). **d**, Quantification of APOE and CTSB immunoreactivities in IBA1$^+$ microglia from different regions of the CNS during development. Bars represent mean ± s.e.m. from four animals (embryonic forebrain, 756 cells; embryonic cerebellum, 541 cells; juvenile cortex, 853 cells; adult cortex, 800 cells). **e**, Distribution of *Cst3* and *Sparc* transcripts in microglia (2,966 cells) on the basis of *t*-SNE plots. Colour keys indicate the expression levels. **f**, Representative immunofluorescence images for CST3, SPARC and IBA1 in the embryonic forebrain and adult cortex. Inset 1 indicates CST3$^+$SPARC$^+$IBA1$^+$ microglia (C9 and C10), and inset 2 highlights CST3$^-$SPARC$^-$IBA1$^+$ microglia (C7) during adulthood. Representative images out of four mice investigated are shown. Scale bars, 50 μm (overview), 20 μm (inset). **g**, Quantification of CST3 and SPARC immunopositivity in microglia from different regions of the CNS at distinct developmental time points. Bars represent mean ± s.e.m. from four animals (embryonic forebrain, 598 cells; juvenile cortex, 1,961 cells; adult cortex, 1,176 cells; embryonic cerebellum, 569 cells; juvenile cerebellum, 620 cells; adult cerebellum, 642 cells).

(Fig. 2b, Extended Data Fig. 2d), We next confirmed the existence of APOE$^+$IBA1$^+$ microglia and cathepsin B (CTSB) $^+$IBA1$^+$ microglia in the embryonic brains by triple immunofluorescence staining of the corresponding proteins (Fig. 2c). These distinct embryonic subpopulations were not observed in the postnatal brains (Fig. 2c, d). On the other hand, the postnatal C9 and C10 clusters were characterized by high levels of expression of *Cst3*—which encodes cystatin C (also known as cystatin 3, CST3), a cysteine proteinase inhibitor that is involved in neurodegenerative diseases of the CNS[1]—and *Sparc* (which encodes 'secreted protein acidic and rich in cysteine') (Fig. 2e). Immunostaining for CST3 and SPARC confirmed the presence of CST3$^+$SPARC$^+$IBA1$^+$ microglia in the postnatal brains, whereas this population was virtually absent from embryonic forebrains (Fig. 2f, g). Expression of CST3 was also detectable in a subpopulation of ALDH1L1$^+$ astrocytes in the adult brain (Extended Data Fig. 3). In the juvenile cortex, almost all microglia expressed CST3 and SPARC (Fig. 2f, g), whereas the abundance of this subpopulation of microglia was slightly diminished in the adult cortex (Fig. 2g). By contrast, the proportion of CST3$^+$SPARC$^+$IBA1$^+$ microglia did not change between the juvenile and adult cerebellum (Fig. 2g), although the overall percentage of SPARC-expressing microglia was lower in the cerebellum than in cortex (Fig. 2g). Taken together, our data identify markers of subsets of microglia and demonstrate the spatiotemporal and phenotypic diversity of these subsets during CNS development and homeostasis in the adult brain.

To determine whether CNS pathology is accompanied by the appearance of disease-specific populations of microglia, we compared a model of toxic demyelination (cuprizone treatment) with the classical model for neurodegeneration (unilateral facial nerve axotomy, FNX) (Extended Data Fig. 1a). The blood–brain barrier remains intact in both models, and a loss of oligodendrocytes in the corpus callosum (with cuprizone treatment) or a remote neurodegeneration within the facial nucleus (with FNX) lead to local microglial activation without recruitment of circulating monocytes[14,15]. The two models enabled us

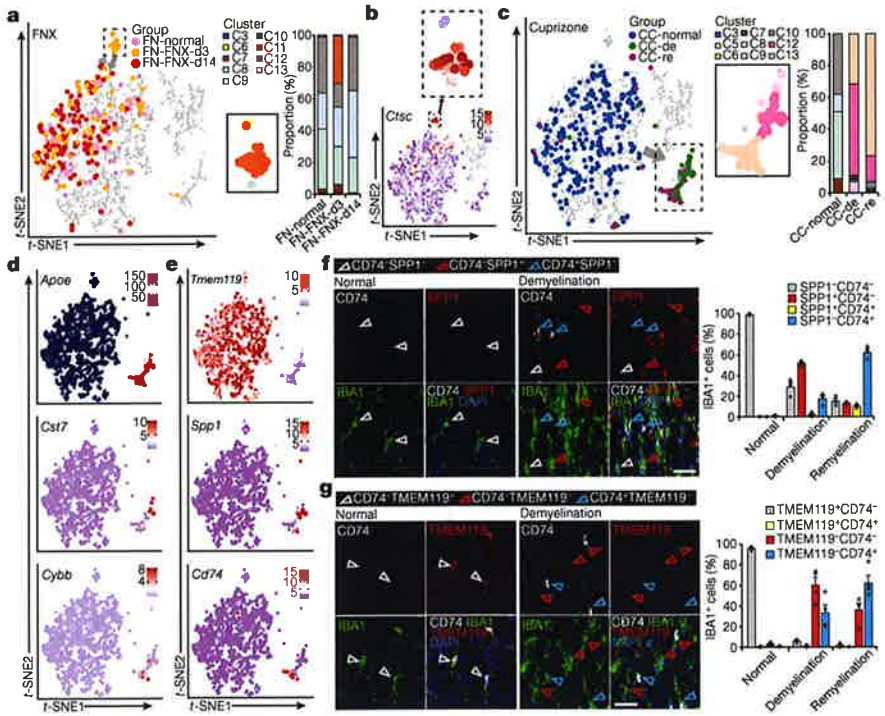

Fig. 3 | Specific disease-associated populations of microglia with distinct kinetics during demyelination and neurodegeneration. **a**, Left, kinetics of facial nucleus (FN) subpopulation of microglia on a *t*-SNE map either untreated (FN-normal), 3 days post FNX (FNX-d3) or 14 days post FNX (FNX-d14). Right, histogram displaying the proportion of clusters of microglia either FN-normal, or after FNX-d3 or FNX-d14. **b**, Clustering of *Ctsc* gene expression after FNX. The colour key indicates the expression levels. Inset, close-up of the C11 cluster. **c**, Persistent transition of corpus callosum (CC) population of microglia on a *t*-SNE map before (CC-normal) and after demyelination (CC-de) or remyelination (CC-re). Close-ups reveal distribution of clusters after demyelination and remyelination. Right, Histogram showing long-lasting changes in populations of microglia after cuprizone treatment. **d**, Kinetics of *Apoe*, *Cst7* and *Cybb* expression after cuprizone challenge, displayed in *t*-SNE plots. Colour keys represent the respective expression levels. **e**, *t*-SNE plots for *Tmem119*, *Spp1* and *Cd74* after cuprizone treatment. Colour keys indicate the expression levels. **f**, **g**, Left, representative immunofluorescence images for SPP1, CD74 and IBA1 (**f**), and TMEM119, CD74 and IBA1 (**g**) in the normal and demyelinated corpus callosum. **f**, Arrowheads indicate $SPP1^-CD74^-IBA1^+$ (white), $SPP1^+CD74^-IBA1^+$ (red) and $SPP1^-CD74^+IBA1^+$ (blue) microglia, respectively. **g**, Arrowheads show $TMEM119^+CD74^-IBA1^+$ (white), $TMEM119^-CD74^-IBA1^+$ (red) and $TMEM119^-CD74^+IBA1^+$ (blue) microglia. Representative pictures out of three or four mice investigated are shown. Right panels show the respective quantification. Bars represent mean ± s.e.m. of 3 to 4 mice (**f**, normal, 825 cells; demyelination, 817 cells; remyelination, 437 cells; **g**, normal, 808 microglia cells; demyelination, 1,024 cells; remyelination, 972 cells). Scale bars, 30 μm.

to study microglial plasticity after withdrawal of cuprizone or during axonal regeneration (Extended Data Fig. 1a).

On the *t*-SNE plot, homeostatic microglia were distributed uniformly in a major population, but cells that clustered separately were found three days after FNX (cluster C11), and in the five-week and ten-week cuprizone treatment groups (clusters C12 and C13) (Extended Data Fig. 4a–c). The distinct C11 cluster of microglia— characterized by strong expression of *Ctsc* (which encodes cathepsin C)—was observed three days after FNX (Fig. 3a, b), whereas microglia in mice 14 days after FNX clustered with the homeostatic microglia population. By contrast, demyelination induced long-lasting transcriptional changes that only slightly recovered at the ten-week time point (Fig. 3c). Collectively, our data suggest that microglia are able to rapidly change their phenotype and gain a discrete context- and time-dependent signature.

Analysis of the disease-specific signatures in microglia revealed that the expression of *Apoe*, *Axl*, *Igf1*, *Lyz2*, *Itgax*, *Gpnmb* and *Apoc1* were induced during both demyelination and remyelination (Fig. 3d, Extended Data Fig. 5a). *Fam20c*, *Cst7*, *Ccl6*, *Fn1*, *Ank*, *Psat1* and *Spp1* were enriched to variable degrees in C12 microglia (Fig. 3d, e, Extended Data Fig. 5b, c, e), whereas the C13 cluster of microglia was characterized by high levels of expression of *Cybb* and the MHC class II genes *Cd74*, *H2-Aa* and *H2-Ab1* (Fig. 3d, e, Extended Data Fig. 5g, i). On the other hand, the microglial marker *Tmem119* was downregulated following cuprizone treatment (Fig. 3e). Single-molecule fluorescence in situ hybridization validated the disease-associated expression of *Fn1*, *Spp1* and *Cybb* transcripts in microglia that express *Cx3cr1* (Extended Data Fig. 5d, f, h). Furthermore, both demyelination-associated ($SPP1^+CD74^-IBA1^+$ and $TMEM119^-CD74^-IBA1^+$) and remyelination-associated ($SPP1^-CD74^+IBA1^+$ and $TMEM119^-CD74^+IBA1^+$) subsets of microglia were confirmed at the protein level by triple immunofluorescence staining (Fig. 3f, g). Overall, our results suggest that unique microglia subpopulations, characterized by distinct signatures, emerge under defined disease conditions.

To extend our studies of microglial heterogeneity from mice to humans, we analysed 1,180 cortical microglia that were isolated from surgically resected human brain tissue without histological evidence of CNS pathology (hereafter referred to as 'healthy') (Supplementary Table. 1). Unbiased hierarchical clustering revealed four major clusters, hereafter referred to as healthy human clusters 1 to 4 (HHu-C1 to HHu-C4) (Extended Data Fig. 6). Detailed analysis of differentially regulated genes revealed similarities with the gene expression profiles of mouse homeostatic microglia. For example, *CST3* (which is enriched in mouse C9 and C10) was more highly expressed in HHu-C1 and HHu-C2 than in HHu-C3 and HHu-C4 (Extended Data Fig. 6f). By contrast, the HHu-C4 cluster showed comparatively high levels of expression of the chemokine genes *CCL4* and *CCL2*, and the zinc finger transcription factors *EGR2* and *EGR3* (Extended Data Fig. 6f). *Ccl4* mRNA was rarely expressed in mouse microglia even after cuprizone treatment (Extended Data Fig. 5j). Notably, *P2RY13* mRNA was highly expressed by the HHu-C1 and HHu-C2 clusters (Extended Data Fig. 6f). Our analysis identified homeostatic human microglia states that have distinct gene expression patterns that partially overlap with those of adult mouse microglia.

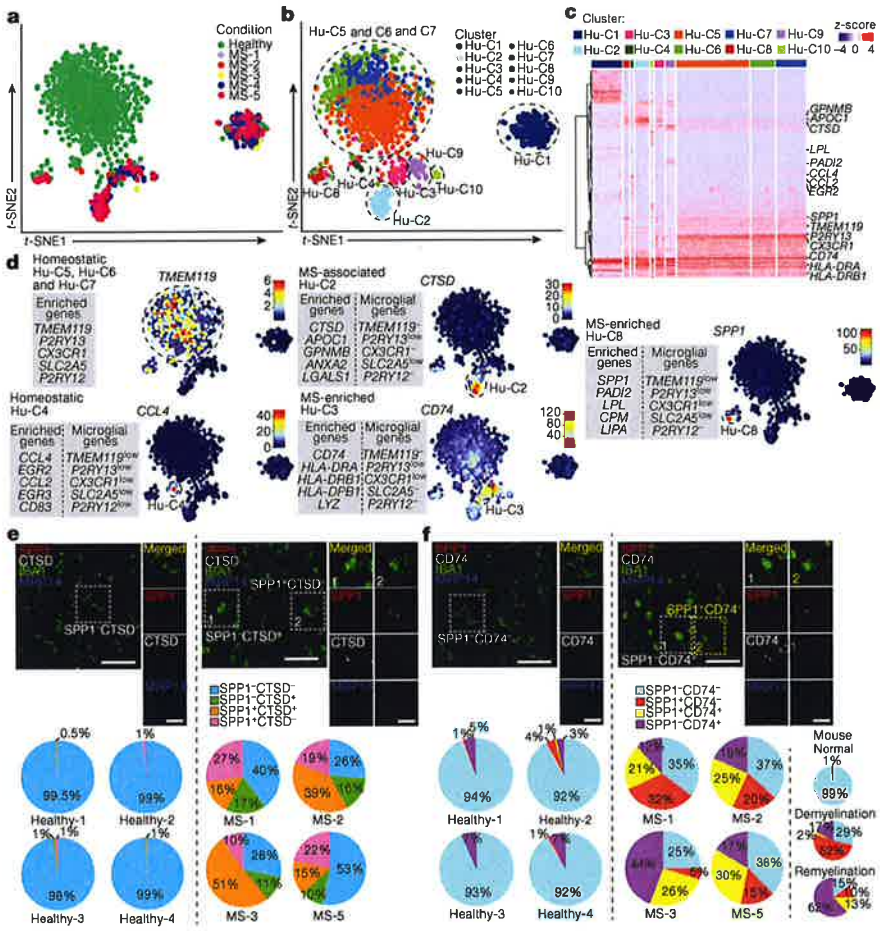

Fig. 4 | Presence of distinct subclasses of microglia in brains of healthy humans and patients with multiple sclerosis. a, *t*-SNE plot of 1,602 individual human microglia isolated from five individual non-pathological brains (healthy) and five patients with early active multiple sclerosis (MS; MS-1 to MS-5). Colours correspond to each condition or patient. **b**, *t*-SNE plot depicting ten major clusters (Hu-C1 to Hu-C10). Colours correspond to each cluster. **c**, Heat map of all differentially regulated genes in each cluster. **d**, *t*-SNE plots of the clusters of microglia, which represent the top five enriched genes for each cluster. **e**, **f**, Top, representative immunofluorescence images for SPP1, CTSD, IBA1 and MRP14 (**e**), and SPP1, CD74, IBA1 and MRP14 (**f**), indicating subsets of microglia in healthy brains (left panels) and brains of patient with multiple sclerosis (right panels). **e**, Insets represent $SPP1^-CTSD^+MRP14^-IBA1^+$ microglia (inset 1) and $SPP1^+CTSD^-MRP14^-IBA1^+$ microglia (inset 2). **f**, Insets indicate $SPP1^-CD74^+MRP14^-IBA1^+$ (white) and $SPP1^+CD74^-MRP14^-IBA1^+$ (yellow) parenchymal microglia, respectively. Representative images out of four individuals are shown. Scale bars, 50 μm (overview), 20 μm (inset). **e**, **f**, Bottom panels show quantification of microglia immunoreactivities in healthy brains or brains from patients with multiple sclerosis. Percentages indicate the relation of $MRP14^-IBA1^+$ subsets of microglia in individual brains. Per patient, 152–200 microglia were examined. **f**, Bottom right, distribution of SPP1- and CD74-reactive $IBA1^+$ subsets of microglia in the healthy mouse corpus callosum or during cuprizone-induced demyelination and remyelination, as shown in Fig. 3f.

Activated microglia have previously been implicated in the disease progression of multiple sclerosis, a debilitating neurological disorder that is associated with demyelination[16]. To examine the presence of subpopulations of human microglia specific to multiple sclerosis, 422 $CD45^+$ cells isolated from the brains of five patients with histologically confirmed early active multiple sclerosis (Extended Data Fig. 7) were subjected to scRNA-seq and subsequently analysed together with healthy human microglia (Fig. 4a–d). Unsupervised clustering grouped the $CD45^+$ cells into ten clusters, which we termed human clusters 1 to 10 (Hu-C1 to Hu-C10) (Fig. 4a–d). Among them, the transcriptome of the Hu-C1 showed a lymphocyte signature (Extended Data Fig. 8a), and the Hu-C9 and Hu-C10 clusters were characterized by a clear monocytic profile (Extended Data Fig. 8a); these clusters were therefore excluded from further analysis. The remaining seven myeloid clusters (Hu-C2 to Hu-C8) expressed microglial core genes, such as *TMEM119* and *P2RY12*, to varying degrees (Fig. 4d). The Hu-C5, Hu-C6 and Hu-C7 clusters, which consisted entirely of microglia from healthy brains, showed the highest levels of expression of the microglial core genes and were therefore considered to represent homeostatic states of microglia (Fig. 4b–d, Extended Data Fig. 8b). The Hu-C4 cluster—which contained microglia from the healthy and diseased brains—was characterized by reduced levels of expression of the core signature genes, but elevated levels of *CCL2*, *CCL4*, *EGR2* and other chemokine and cytokine genes, which suggests that these microglia were pre-activated (Fig. 4d, Extended Data Fig. 8e). Two clusters of microglia that were enriched in brains of patients with multiple sclerosis (Hu-C3 and Hu-C8), and one cluster of microglia that was associated with multiple sclerosis (Hu-C2), were clearly separated from the homeostatic clouds on *t*-SNE plots (Fig. 4b–d). The Hu-C2, Hu-C3 and Hu-C8 clusters showed an increased level of expression of *APOE* and *MAFB* (Extended Data Fig. 8g), whereas the expression of microglial core genes was downregulated or even absent (Fig. 4d). The strong reduction of TMEM119 expression in microglia in demyelinating lesions of brains from patients with multiple sclerosis was confirmed histologically (Extended Data Fig. 8i). The Hu-C2 cluster was characterized by high levels of expression of *CTSD*, *APOC1*, *GPNMB*, *ANXA2* and *LGALS1* (Fig. 4d, Extended Data Fig. 8c). Hu-C3 microglia showed increased gene expression of MHC class II-related molecules, such as *CD74*, *HLA-DRA*, *HLA-DRB1* and *HLA-DPB1* (Fig. 4d, Extended Data Fig. 8d). This suggests an immunoregulatory role, reminiscent of the subtype (C13) of microglia associated with remyelination in mice

(Fig. 3). Finally, Hu-C8 microglia showed strong expression of *SPP1*, *PADI2* and *LPL* genes, similar to the C12 microglia associated with demyelination in mice (Fig. 4d, Extended Data Fig. 8f). Of note, canonical correlation analysis of mouse and human microglia orthologues confirmed that clusters of microglia (Hu-C2, Hu-C3 and Hu-C8) that are enriched in or associated with the brains of patients with multiple sclerosis have a gene expression profile that is similar to that of clusters of microglia associated with demyelination (C12) and remyelination (C13) in mice (Extended Data Fig. 9).

To validate our scRNA-seq results histologically, we first stained brain sections from patients with multiple sclerosis for MRP14, which is known to label infiltrating monocytes but not microglia in early active lesions[17]. Human brain sections without CNS pathology were virtually devoid of $MRP14^+IBA1^+$ cells, whereas approximately 12% of $IBA1^+$ cells in the brain sections from patients with multiple sclerosis were infiltrating monocytes (Extended Data Fig. 8j), which indicates that the vast majority of $IBA1^+$ cells in these sections were resident $MRP14^-IBA1^+$ microglia. Triple immunofluorescence staining identified $CTSD^+MRP14^-IBA1^+$, $SPP1^+MRP14^-IBA1^+$ and $CD74^+MRP14^-IBA1^+$ subsets of microglia as part of the Hu-C2, Hu-C8 and Hu-C3 clusters in brain sections from patients with multiple sclerosis (Fig. 4e, f). In contrast to the mouse cuprizone-induced demyelination model, the proportion of SPP1-, CTSD- and CD74-expressing subsets of microglia varied substantially between individual patients with multiple sclerosis (Fig. 4e, f), which indicates high inter-individual heterogeneity. Together, these findings suggest the existence of distinct disease-related subtypes of microglia in the brains of patients with multiple sclerosis, and that these microglia are phenotypically similar to subtypes of mouse microglia in a demyelination model.

Previous studies of regional variations in mice of microglial density[18], surface expression of a small panel of immune molecules[19], dependency on interleukin-34[20,21], electrophysiological features[22], phagocytic activity[23] and microarray analysis of microglial bulk RNA[11] or scRNA-seq[24] have suggested diversity of microglia. To our knowledge, our study provides the first in vivo comparison of microglia heterogeneity at a single-cell resolution in the mouse and human CNS (Extended Data Fig. 10). Although we detected transcriptionally distinguishable subpopulations of microglia during homeostasis, these did not appear as distinct clusters but rather as a transcriptional continuum of the local population of microglia. This might reflect the transcriptional basis for the ability of microglia to swiftly adapt to changing environmental cues. Our data further indicate that microglial responses to pathology are not uniform, but are shaped by the underlying pathology. Specifically, we found disease-associated subtypes of microglia that differed between neurodegenerative conditions and toxic demyelination. The appearance of context-dependent subtypes of microglia with their own specific transcriptional profiles has the potential to reveal new therapeutic targets. Moreover, by establishing the transcriptional profile of heterogeneous populations of microglia in healthy and diseased rodents and humans, our study may provide insights into the pathogenesis of CNS diseases.

Online content

Any methods, additional references, Nature Research reporting summaries, source data, statements of data availability and associated accession codes are available at https://doi.org/10.1038/s41586-019-0924-x.

Received: 1 February 2018; Accepted: 11 January 2019;
Published online 13 February 2019.

1. Prinz, M. & Priller, J. Microglia and brain macrophages in the molecular age: from origin to neuropsychiatric disease. *Nat. Rev. Neurosci.* **15**, 300–312 (2014).
2. Colonna, M. & Butovsky, O. Microglia function in the central nervous system during health and neurodegeneration. *Annu. Rev. Immunol.* **35**, 441–468 (2017).
3. Herz, J., Filiano, A. J., Smith, A., Yogev, N. & Kipnis, J. Myeloid cells in the central nervous system. *Immunity* **46**, 943–956 (2017).
4. Prinz, M., Erny, D. & Hagemeyer, N. Ontogeny and homeostasis of CNS myeloid cells. *Nat. Immunol.* **18**, 385–392 (2017).
5. Kierdorf, K. et al. Microglia emerge from erythromyeloid precursors via Pu.1- and Irf8-dependent pathways. *Nat. Neurosci.* **16**, 273–280 (2013).
6. Hagemeyer, N. et al. Microglia contribute to normal myelinogenesis and to oligodendrocyte progenitor maintenance during adulthood. *Acta Neuropathol.* **134**, 441–458 (2017).
7. Matcovitch-Natan, O. et al. Microglia development follows a stepwise program to regulate brain homeostasis. *Science* **353**, aad8670 (2016).
8. Mathys, H. et al. Temporal tracking of microglia activation in neurodegeneration at single-cell resolution. *Cell Reports* **21**, 366–380 (2017).
9. Jordao, M. J. et al. Single-cell profiling identifies myeloid cell subsets with distinct fates during neuroinflammation. *Science* **363**, eaat7554 (2019).
10. Keren-Shaul, H. et al. A unique microglia type associated with restricting development of Alzheimer's disease. *Cell* **169**, 1276–1290 (2017).
11. Grabert, K. et al. Microglial brain region-dependent diversity and selective regional sensitivities to aging. *Nat. Neurosci.* **19**, 504–516 (2016).
12. Herman, J. S., Sagar, & Grün, D. FateID infers cell fate bias in multipotent progenitors from single-cell RNA-seq data. *Nat. Methods* **15**, 379–386 (2018).
13. Krasemann, S. et al. The TREM2–APOE pathway drives the transcriptional phenotype of dysfunctional microglia in neurodegenerative diseases. *Immunity* **47**, 566–581.e9 (2017).
14. Tay, T. L. et al. A new fate mapping system reveals context-dependent random or clonal expansion of microglia. *Nat. Neurosci.* **20**, 793–803 (2017).
15. Mildner, A. et al. Microglia in the adult brain arise from $Ly\text{-}6C^{hi}CCR2^+$ monocytes only under defined host conditions. *Nat. Neurosci.* **10**, 1544–1553 (2007).
16. Benveniste, E. N. Role of macrophages/microglia in multiple sclerosis and experimental allergic encephalomyelitis. *J. Mol. Med. (Berl.)* **75**, 165–173 (1997).
17. Brück, W. et al. Monocyte/macrophage differentiation in early multiple sclerosis lesions. *Ann. Neurol.* **38**, 788–796 (1995).
18. Lawson, L. J., Perry, V. H. & Gordon, S. Turnover of resident microglia in the normal adult mouse brain. *Neuroscience* **48**, 405–415 (1992).
19. Doorn, K. J. et al. Brain region-specific gene expression profiles in freshly isolated rat microglia. *Front. Cell. Neurosci.* **9**, 84 (2015).
20. Wang, Y. et al. IL-34 is a tissue-restricted ligand of CSF1R required for the development of Langerhans cells and microglia. *Nat. Immunol.* **13**, 753–760 (2012).
21. Greter, M. et al. Stroma-derived interleukin-34 controls the development and maintenance of Langerhans cells and the maintenance of microglia. *Immunity* **37**, 1050–1060 (2012).
22. De Biase, L. M. et al. Local cues establish and maintain region-specific phenotypes of basal ganglia microglia. *Neuron* **95**, 341–356.e6 (2017).
23. Ayata, P. et al. Epigenetic regulation of brain region-specific microglia clearance activity. *Nat. Neurosci.* **21**, 1049–1060 (2018).
24. Hammond, T. R. et al. Single-cell RNA sequencing of microglia throughout the mouse lifespan and in the injured brain reveals complex cell-state changes. *Immunity* **50**, 253–271.e6 (2019).

Acknowledgements We thank M. Ditter, E. Barleon, T. el Gaz and J. Bodinek-Wersing for technical assistance; C. Gross for proofreading; N. Mossadegh for helpful discussions; and A. Zeisel and S. Linnarsson (Karolinska Institute, Sweden) for sharing data and support. The samples and data used for this project were kindly provided by the West German Biobank. T.M. was supported by the KANAE Foundation and the Japan Society for the Promotion of Science. M.P. is supported by the Sobek Foundation, the Ernst-Jung Foundation, the DFG (SFB 992, SFB1160, SFB/TRR167, Reinhart Koselleck Grant), the Ministry of Science, Research and Arts, Baden-Wuerttemberg (Sonderlinie 'Neuroinflammation') and the BMBF-funded competence network of multiple sclerosis (KKNMS). This study was supported by the DFG under Germany's Excellence Strategy (CIBSS – EXC-2189 – Project ID390939984). S. is supported by the DFG (GR4980) the Behrens-Weise-Foundation, and the Max Planck Society. D.G. is supported by the Max Planck Society. J.P. is supported by the DFG (SFB/TRR167 B05 and B07), BIH CRG 2a, and the UK DRI Momentum Award. C. Stadelmann is supported by the DFG (STA1389/2-1), the Deutsche Multiple Sklerose Gesellschaft (DMSG), the National MS Society of the USA (NMSS) and the Hertie Foundation. C.B. is supported by the DFG (SFB/TRR167 B05).

Reviewer information *Nature* thanks Arnold Kriegstein and the other anonymous reviewer(s) for their contribution to the peer review of this work.

Author contributions T.M., R.S., O.S., C.B., L.A., C. Scheiwe, S.N., P.K., G.v.L., V.A.C., P.C.R., A.M., U.S. and R.G. conducted experiments and analysed the data. M.P., C. Stadelmann and J.P. analysed the data, contributed to the in vivo studies and provided mice or reagents. D.G. and S. established the sequencing platform, supervised the sequencing and helped with bioinformatics. T.M. and M.P. supervised the project and wrote the manuscript.

Competing interests The authors declare no competing interests.

Additional information
Extended data is available for this paper at https://doi.org/10.1038/s41586-019-0924-x.
Supplementary information is available for this paper at https://doi.org/10.1038/s41586-019-0924-x.
Reprints and permissions information is available at http://www.nature.com/reprints.
Correspondence and requests for materials should be addressed to M.P.
Publisher's note: Springer Nature remains neutral with regard to jurisdictional claims in published maps and institutional affiliations.

METHODS

No statistical methods were used to predetermine sample size. The experiments were not randomized and investigators were not blinded to allocation during experiments and outcome assessment.

Mice. CD-1 mice were used. All animal experiments were approved by local administration and were performed in accordance to the respective national, federal and institutional regulations. Detailed mouse information is provided in Supplementary Table 1.

scRNA-seq for mouse microglia. Microglia were FACS-sorted from up to six different regions of the CNS of healthy and diseased brains (see gating strategy shown in Supplementary Fig. 1) into a 384-well plate containing a lysis buffer, and were analysed using the Smart-seq2 method. Expression profiles were obtained as absolute cDNA molecule counts using the STAR aligner[25] to align raw sequences in conjunction with feature Counts (part of the subread package)[26] to obtain gene counts. Further analysis and data normalization was performed using the RaceID package[12]. Clusters with more than ten individual cells were retained for further analysis, and normalized to transcripts per million to compensate for differences in total transcriptome size between cell types. Heat maps were generated using online software[27].

Analysis of microglia from human brains. All experiments with human materials were approved by the local administration and were performed in accordance with the respective national, federal and institutional regulations. Human microglia were isolated from histologically healthy brain tissue removed during brain surgery for the treatment of epilepsy in five individuals (these tissues are not part of the epileptic region but are routinely removed to surgically access the epileptic lesion). Histopathological changes were excluded by an experienced neuropathologist, and only histologically healthy specimens were included in this study. $CD45^+$ cells including microglia were FACS-sorted into a 384-well plate containing lysis buffer. scRNA-seq was conducted using the Cel-Seq2 protocol and processed as previously described[28]. Libraries were sequenced on an Illumina HiSeq 3000 System in high-output run mode at a depth of ~200,000 reads per cell. Paired-end reads were aligned to the transcriptome using bwa with default parameters, and all isoforms of the gene were counted to a single gene locus[29]. Reads that were not uniquely mapped were discarded. The left read contained the barcode information (6 bases corresponding to unique molecular identifier (UMI) plus 6 bases that represented the cell-specific barcode and a polyT stretch), and was omitted from quantification. The corresponding right read was mapped to the ensemble of all gene loci and used for quantification. Genes were counted on the basis of the number of UMIs per transcript from a given gene locus. The number of UMIs was converted to transcript counts based on a negative binomial distribution[30]. The aggregate of transcript counts with the same cell barcode represented the transcriptome of an individual cell. Data analysis, normalization and visualization was performed using the RaceID2 package[31]. Clusters with more than 15 individual cells were retained for further analysis and transcript counts were normalized by down sampling to 1,500. Detailed human patient information is provided in Supplementary Table 1.

Flow cytometry. After transcardial perfusion with PBS, brains were roughly minced and homogenized with a potter in HBSS containing 15 mM HEPES buffer and 0.54% glucose. Whole-brain homogenate was separated by 70/37/30% layered Percoll gradient centrifugation at 800*g* for 30 min at 4 °C (no brake). The CNS macrophages containing interphase were then collected and washed once with PBS containing 2% FCS and 10 mM EDTA before staining. Cells were stained with primary antibodies directed against CD11b (M1/70, BioLegend), CD45 (30-F11, BD Biosciences), Ly6C (AL-21, BD Biosciences) and Ly6G (1A8, BD Biosciences) for 20 min, and CD206 (C068C2, BioLegend) for 45 min at 4 °C. After washing, cells were sorted using a MoFlo Astrios (Beckman Coulter). Viable cells were gated by staining with Fixable Viability Dye (eBioscience). Data were acquired with Summit software (Becton Dickinson). Post-acquisition analysis was performed using FlowJo software, version X.0.7.

Immunohistochemistry and cell quantifications. For juvenile and adult mice, after transcardial perfusion with PBS, brains were fixed for 4 h in 4% PFA, dehydrated in 30% sucrose and embedded in Tissue-Tek O.C.T. compound (Sakura Finetek Germany GmbH). For embryos, isolated brains were fixed for 4 h in 4% PFA, dehydrated in 30% sucrose and embedded in Tissue-Tek O.C.T. compound. Cryosections were obtained as previously described[32]. Sections were then blocked with PBS containing 5% bovine serum albumin and permeabilized with 0.1% Triton-X 100 in blocking solution. Primary antibodies were added over night at a dilution of 1:500 for IBA1 (ab178846, Abcam), 1:200 for APOE (AB947, Millipore), 1:200 for CTSB (ab58802, Abcam), 1:200 for CST3 (AF1238, R&D Systems), 1:200 for SPARC (IC942G, R&D Systems), 1:400 for NeuN (MAB377, Millipore), 1:1,000 for APC (OB80, Millipore), 1:100 for ALDH1L1 (ab87117, Abcam), 1:500 for TMEM119 (ab209064, Abcam), 1:500 for SPP1 (ab8448, Abcam) and 1:200 for CD74 (In1/CD74, BioLegend), at 4 °C. Secondary antibodies were purchased from Thermo Fisher Scientific added as follows: Alexa Fluor 488 1:500, Alexa Fluor 568 1:500 and Alexa Fluor 647 1:500 for 2h at room temperature. Human tissue blocks were fixed in 4% PFA overnight and embedded in paraffin. Sections were then blocked with PBS containing 5% bovine serum albumin and permeabilized with 0.1% Triton-X 100 in blocking solution. Primary antibodies were treated over night at a dilution of 1:500 for IBA1 (ab178846, Abcam; ab139590, Abcam; NB100-1028, Novus Biologicals), 1:200 for SPP1 (HPA027541, Sigma), 1:500 for CD74 (ab9514, Abcam), 1:500 for CTSD (ab6313, Abcam) and 1:200 for MRP14 (T-1026, BMA Biomedicals; LS-B12844, LSBio). Secondary antibodies were purchased from Thermo Fisher Scientific added as follows: Alexa Fluor 405 1:500, Alexa Fluor 488 1:500, Alexa Fluor 568 1:500 and Alexa Fluor 647 1:500 for 2 h, at room temperature. Coverslips were mounted with/without ProLong Diamond Antifade Mountant with DAPI (Thermo Fisher Scientific). Images were taken using a conventional fluorescence microscope (Olympus BX-61 with a colour camera (Olympus DP71) or BZ-9000 (Keyence)) and the confocal pictures were taken with Fluoview FV 1000 (Olympus) using a 20 × 0.95 NA (XLUMPlanFL N, Olympus).

Facial nerve axotomy and cuprizone model of demyelination and remyelination. Facial nerve was injured as previously described[14,15]. In brief, mice were anaesthetized by subcutaneous injection of a mixture of ketamine (50 mg/kg) and xylazine (7.5 mg/kg), and the right facial nerve was transected at the stylomastoid foramen, resulting in ipsilateral whisker paresis. Cuprizone treatment was used as a model of toxic demyelination and remyelination[15,33]. For demyelination, mice were fed for 5 weeks with 0.45% (wt/wt) cuprizone (Sigma) in the ground breeder chow. For remyelination, the cuprizone diet was discontinued after five weeks and animals were maintained for further five weeks under normal diet to allow spontaneous remyelination. Untreated age-matched mice were used as control.

Single-molecule fluorescent in situ hybridization. Mice were perfused with PBS, followed by 4% paraformaldehyde (PFA). The brain tissues were collected and immersion-fixed in 4% PFA for 3 h, and subsequently were put into 30% sucrose in 4% PFA at 4 °C overnight, and embedded in OCT for sectioning, frozen on dry ice and stored at −80 °C until used. Ten-micrometre-thick sections mounted on the glass plate were washed 3 times with PBS, and treated with pre-chilled methanol for 10 min at −20 °C. Then, the slides were incubated for 10 min at 70 °C in Tris-EDTA (pH 8.0), and the sections were washed with SSC 2× and incubated for 4 h with hybridization buffer containing 250 nM fluorescent label probes (LGC Biosearch Technologies) at 38.5 °C. After 4 washes with 20% formamide wash buffer containing SSC 2×, the slides were mounted with Prolong Gold containing DAPI. Stack images were taken using a Olympus BX-61 microscope.

Canonical correlation analysis. Comparisons between human and mouse data were performed by initially determining differentially expressed genes with RaceID by testing for differences between individual clusters versus all other steady-state or disease associated clusters. Genes found to be differentially expressed by in any of these comparisons (adjusted $P < 0.01$, fold change (expressed in $\log_2$) > 1) were selected for further analysis. For genes from the human dataset, mouse orthologues were identified from the NCBI HomoloGene database (https://www.ncbi.nlm.nih.gov/homologene) using the annotationTools R package[34]; the same was done to identify human orthologues for the mouse genes. All human genes with an orthologue in the mouse set, as well as all mouse genes with an orthologue in the human set, were kept. Canonical cluster analysis as implemented in the Seurat package[35] was then performed on the 768 common genes identified in this manner.

Reporting summary. Further information on research design is available in the Nature Research Reporting Summary linked to this article.

Data availability

Raw data for mouse and human single cell RNA-sequencing have been deposited in the Gene Expression Omnibus, and are available at the following accession numbers: GSE120629 (mouse), GSE120747 (mouse) and GSE124335 (human). All other data are available from the corresponding author on reasonable request.

25. Dobin, A. et al. STAR: ultrafast universal RNA-seq aligner *Bioinformatics* **29**, 15–21 (2013).
26. Liao, Y., Smyth, G. K. & Shi, W. The Subread aligner: fast, accurate and scalable read mapping by seed-and-vote. *Nucleic Acids Res.* **41**, e108 (2013).
27. Gu, Z., Eils, R. & Schlesner, M. Complex heatmaps reveal patterns and correlations in multidimensional genomic data. *Bioinformatics* **32**, 2847–2849 (2016).
28. Hashimshony, T. et al. CEL-Seq2: sensitive highly-multiplexed single-cell RNA-seq. *Genome Biol.* **17**, 77 (2016).
29. Li, H. & Durbin, R. Fast and accurate long-read alignment with Burrows–Wheeler transform. *Bioinformatics* **26**, 589–595 (2010).
30. Grün, D., Kester, L. & van Oudenaarden, A. Validation of noise models for single-cell transcriptomics. *Nat. Methods* **11**, 637–640 (2014).
31. Grün, D. et al. Single-cell messenger RNA sequencing reveals rare intestinal types. *Nature* **525**, 251–255 (2015).
32. Goldmann, T. et al. USP18 lack in microglia causes destructive interferonopathy of the mouse brain. *EMBO J.* **34**, 1612–1629 (2015).

33. Raasch, J. et al. IκB kinase 2 determines oligodendrocyte loss by non-cell-autonomous activation of NF-κB in the central nervous system. *Brain* **134**, 1184–1198 (2011).
34. Kuhn, A., Luthi-Carter, R. & Delorenzi, M. Cross-species and cross-platform gene expression studies with Bioconductor-compliant R package 'annotationTools'. *BMC Bioinformatics* **9**, 26 (2008).
35. Butler, A., Hoffman, P., Smibert, P., Papalexi, E. & Satija, R. Integrating single-cell transcriptomic data across different conditions, technologies, and species. *Nat. Biotechnol.* **36**, 411–420 (2018).
36. Lucchinetti, C. et al. Heterogeneity of multiple sclerosis lesions: implications for the pathogenesis of demyelination. *Ann. Neurol.* **47**, 707–717 (2000).